

Location-based Real-time Utilization of Reconfigurable Intelligent Surfaces for mmWave Communication and Sensing in Full-Immersive Multiuser VR

*Filip Lemic¹, Jalal Jalali², Gerard Calvo Bartra¹, Alejandro Amat¹,
Jakob Struye², Jeroen Famaey², Xavier Costa Perez¹³⁴*

¹i2Cat Foundation, Spain

²University of Antwerp - imec, Belgium

³NEC Labs Europe GmbH, Germany

⁴ICREA, Spain

Contents

1	Introduction	3
1.1	Structure	4
2	Background, State-of-the-Art, and Challenges	5
2.1	Communication Challenges in VR	5
2.2	Reconfigurable Intelligent Surfaces	6
2.3	Real-Time Sensing for Enhanced Experiences	7
3	Overcoming Communication and Sensing Challenges	9
3.1	Considered Scenario	9
3.2	Location-based RIS Resource Allocation for Communication and Sensing	10
3.2.1	AP Transmit Power Control	13
3.2.2	Location-based Allocation of RIS Elements	13
3.2.3	RIS Passive Beamforming and Radiation Pattern Optimization	14
3.3	Computational Complexity and Convergence Analysis	14
4	Context-Aware RIS Utilization Performance	16
4.1	Evaluation Setup	16
4.2	Evaluation Results	18
4.2.1	Communication and Active Sensing Coverage, and Active Sensing Accuracy . .	18
4.2.2	Advanced Sensing Accuracy	19
5	Conclusions and Implications	22

Abstract

The rapid progression of high-speed communication and computing is ushering an era of deeper interactions in fully immersive virtual worlds. Advancements in technologies like Virtual Reality (VR) and high-frequency wireless communication networks, particularly in millimeter Wave (mmWave) bands, are paving the way for next-generation visualization and interaction platforms. These systems will empower users to navigate virtual environments seamlessly, receiving high-quality, real-time content via mmWave communication networks. In this landscape, Joint Communication and Sensing (JCAS) emerges as a concept within 6G research on wireless communications. It leverages existing wireless communication infrastructures, such as mobile networks and WiFi, for both data transmission and sensing purposes. By utilizing wireless signals as illuminators and analyzing their reflections from users and objects, JCAS enhances situational awareness and enables functionalities like position estimation or target detection.

Toward addressing Quality of Service (QoS) challenges in VR-supporting mmWave networks, Reconfigurable Intelligent Surfaces (RISs) are proposed as a potential solution. These surfaces consist of passive elements capable of dynamically adjusting Electromagnetic (EM) wave phases. Strategically deploying RIS in wireless environments enhances signal strength, reduces path loss, and optimizes overall communication performance. However, the comprehensive evaluation of RIS deployments on the system level remains relatively unexplored. Given the impracticality of field experiments, computer simulations offer a viable means to assess RIS performance. Fortunately, novel end-to-end simulation frameworks have been developed, based on the ns-3 simulator, aiming at optimizing RIS deployment for optimizing both throughput and Signal-to-Noise Ratio (SNR) for each user location in a VR context. By simulating scenarios with and without RISs, their effectiveness in supporting JCAS communications and sensing tasks is demonstrated for the next generation of VR platforms with multiple coexisting users.

1 Introduction

Virtual Reality (VR) is anticipated to transform our digital interactions in various domains, such as healthcare, tourism, education, entertainment, and occupational safety [1]. The advancement of VR relies on enhancing the quality of video content presented to VR users [2] and enabling collaborative multi-user experiences, where the users can interact and cooperate within the virtual realm [3] in real-time. VR systems are poised to accommodate multiple fully-immersed users who can freely navigate their Virtual Experiences (VEs) in indoor environments.

Advanced Machine Learning (ML)-enabled wireless communication networks will be essential for the enablement of the above applications, primarily operating in the millimeter Wave (mmWave) frequency bands, spanning from 30 to 300 GHz [4]. These networks will utilize highly directional transmission and reception capabilities to ensure seamless real-time delivery of high-quality video, audio, and tactile content to mobile VR users [4]. These directional mmWave beams are also expected to continuously track users' movements to maintain Line-of-Sight (LoS) connectivity, thus optimizing Quality of Service (QoS). Simultaneously, the concept of ML-based Redirected Walking (RDW) is being explored to prevent collisions among co-located users and between users and the boundaries of confined VR environments [3]. This approach allows the users to move freely within the virtual realms while discreetly guiding them within the physical setups to avoid collisions, enhancing the overall immersion in the VEs.

The interactive multi-user VE envisions truthfully reproducing the actions of one user in the VEs of the other, potentially collocated, users. Such interaction should be reproduced within the *motion-to-photon* latency of less than 20 ms to avoid causing nausea to the users [5]. Such motion capturing is traditionally performed using cameras strategically positioned in the environment [6]. However, such approaches by-design do not guarantee privacy preservation and induce significant delays due to cross-layer information collection and image processing overheads. More recently, high-frequency Joint Communication and Sensing (JCAS) approaches have gained traction, in which the same communication wavefront is envisioned to be utilized for both tracking of the users and high throughput communication with them [7]. At the same time, passive sensing in the form of mmWave radar is envisaged to be employed for more advanced sensing tasks such as users' motion recognition or 3-Dimensional (3D) pose estimation [8].

In full-immersive VR applications, maintaining stable throughput is of prime importance for maintaining the users' QoS throughout their VEs. At the same time, active JCAS sensing tasks require the maximization of the Signal-to-Noise Ratio (SNR) of the communication wavefront for accuracy maximization, while simultaneously minimizing its variability [7]. These challenging requirements cannot be achieved with existing mmWave hardware such as IEEE 802.11ad/ay Access Points (APs), primarily due to the low number of antenna elements in the practical realization of mmWave transceivers, causing unequal coverage in the deployment environment, as will be demonstrated in the Chapter. An additional challenge comes from the fact that LoS communication with the users might be interrupted due to the presence of multiple users in the deployment environment, causing significant throughput and SNR degradation.

To enable cost-effective indoor VEs, Reconfigurable Intelligent Surfaces (RISs) on or acting as walls are considered as a promising potential solution [2]. A RIS consists of large arrays of passive reflecting elements on a reconfigurable planar surface. These elements can independently modify the phase of an incoming signal before reflecting it towards its intended receiver. The RIS can be a tool for mitigating the users experiencing significant path loss or blockage on the direct link, especially when primarily operating in the mmWave frequency band, as the RIS creates additional propagation pathways - reflected channels [9]. Moreover, the RIS offers added degrees of freedom through the phase shifts of the reflective elements, which can be harnessed to minimize interference [10], [11]. It is also worth noting that RISs are envisioned to be manufactured as passive, cheap, and flexible entities adaptable for indoor VR streaming setups, as they could be used as "soft" and flexible environmental boundaries with no hazard in case of the user collision [12].

In this Chapter, a RIS-supported multiuser mmWave VR environment is considered, where the RISs are deployed on the outer walls and a multi-antenna AP transmits data to a set of single-antenna Head Mounted Devices (HMDs) via the RISs. For the considered scenario, the aggregate data rate of all HMDs is maximized by optimizing the resource allocation of the RIS, beamforming, phase shifts, and radiation patterns as a function of VR users' trajectory (modeled using RDW) in a confined indoor environment. In particular, a resource allocation algorithm is designed to maximize

the system's sum data-rate subject to peak transmit power feasibility and QoS constraints.

The formulated problem is non-convex, thus an Alternative Optimization (AO) algorithm is employed, segmenting the main optimization problem into four distinct sub-problems, followed by optimally solving each sub-problem. For the first sub-problem, i.e., the active beamforming at the AP, the Maximum-Ratio Transmission (MRT) is proved to be the optimal AP beamformer. In the second sub-problem, a closed-form optimal solution is obtained for the RIS phase shifts design using quadratic transformation. A global optimization of the RIS' placement is carried out in the third sub-problem based on a first-order derivative of the objective function. Finally, the optimal radiation pattern is determined in a closed-form format based on the monotonicity of the transformed objective function.

The ns-3 simulation results indicate that RIS with passive beamforming and location-based RIS element allocation, combined with an optimal beamforming at the AP, can achieve improved communication data-rates compared to a number of baseline schemes. Moreover, the results indicate that location-based allocation of RIS elements can be beneficial for various active and passive sensing tasks performed by the network. In particular, RISs are demonstrated to be beneficial for maintaining stable SNR of the communication waveform, which is beneficial on active sensing tasks piggybacking on the communication waveform, such as user localization or tracking. In addition, it has been shown that RISs can be utilized for the optimization of more advanced sensing tasks in which the users are considered as passive sensing targets, such as user gesture recognition or capturing their full volumetric representations. In more general terms, several system-level benefits of context-aware utilization of RISs for optimizing JCAS tasks in VR-supporting multiuser mmWave networks have been showcased.

1.1 Structure

The structure of this Chapter is as follows. Section 2 provides an overview of related works and efforts. Section 3 outlines the adopted system model and presents an analytical characterization of the channel for RIS and its optimal location-based element allocation. Section 4 describes the utilized simulation methodology and outlines how well the presented approach performs in various simulated scenarios. Finally, Section 5 concludes the Chapter.

2 Background, State-of-the-Art, and Challenges

2.1 Communication Challenges in VR

Forthcoming VR systems are envisioned to host multiple users simultaneously, engaging them in interactive VEs in which one user's actions influence the VE of other users, who may be physically co-located or remote. An additional goal is to sustain seamless immersion in VEs while ensuring uninhibited user movement within a tracking area, devoid of collisions with obstructions, environmental confines, or fellow users [13].

The prospective ability to facilitate the engagement of numerous users within interactive VEs will rely on advanced high-frequency wireless networks primarily operating in the mmWave spectrum, spanning from 30 to 300 GHz [14]. Given the high path loss when using these frequencies, it is paramount that APs and HMDs-supporting User Equipments (UEs) focus their energy towards each other, transmitting and receiving highly directionally, through a process called *beamforming* [15], [16]. This way, high-quality VR content can be delivered consistently and in real-time over high-gain links. In the VR scenario, directional mmWave beams should dynamically track users' movements during transmission, preserving LoS connections [5]. Additionally, RDW will be harnessed to avert physical clashes between users and VR setup boundaries or collocated users, allowing them to explore the VE freely while subtly adjusting their paths to prevent collisions, thereby enhancing the sense of immersion [17].

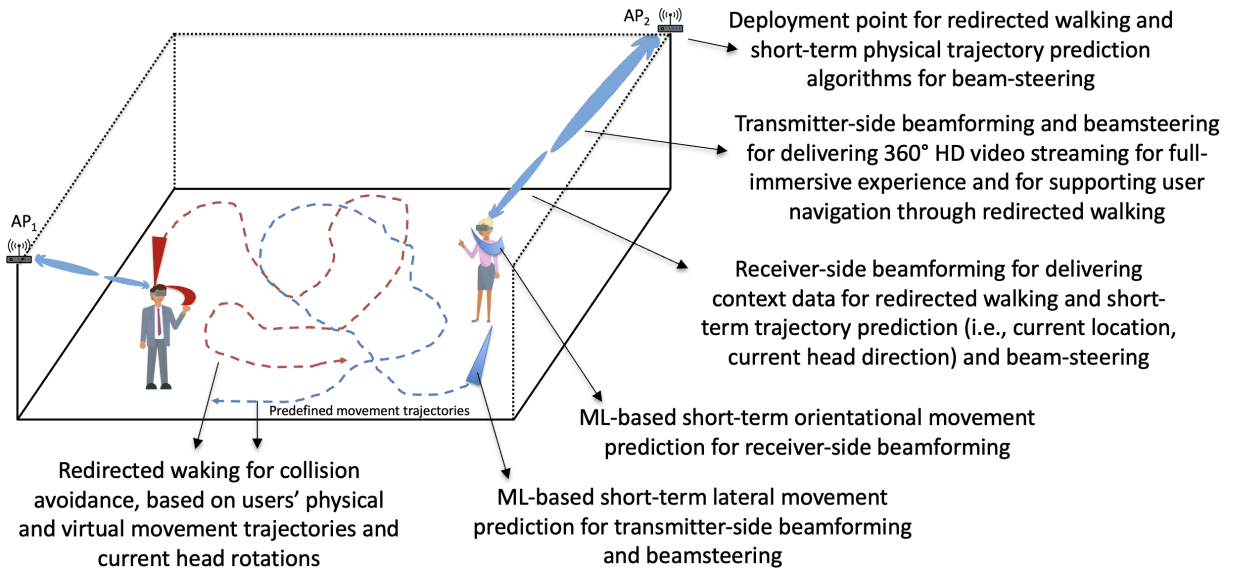


Figure 1: Full-immersive multiuser virtual reality with redirected walking [4]

Accurate short-term prediction of users' movements, both laterally and orientationally, are needed to ensure a convincing experience on several fronts [18], [19]. This enables not only accurate generation of content and proactive RDW [4], but also successful beamforming at both AP and HMD, as motion may be too sudden to allow for reactive beamforming [20]. To cater to this requirement, adaptable coverage proves invaluable for receiver-side beamforming on an HMD, as the slightest misalignment in beam orientation can noticeably impact the SNR [21]. Thus, a flexible beam stretching in the direction of HMD rotation can offer consistently high gain, essential for uninterrupted content delivery [5]. This strategy guarantees that user motion is promptly portrayed on-screen. Ideally this should happen within the 20 ms *motion-to-photon* latency bound, which is the maximal delay between a user's movement and the updated visual response they see on the screen that does not cause discomfort or nausea [14]. The above requirements highlight the necessity of maintaining stable communication coverage across an entire deployment environment. This is explored in detail in this Chapter, and addressed through the location-based utilization of the RIS. A high-level system summary based on the above text is depicted in Figure 1.

A common method to enhance immersion in VEs involves directly mirroring users' physical movements within the VEs [22]. However, this approach typically confines users to limited tracking

spaces, reducing overall immersion. To tackle this limitation, researchers have proposed diverse virtual locomotion techniques to facilitate movement across expansive VEs, even within confined tracking areas.

Leading-edge techniques leverage gestures resembling walking (e.g., walking-in-place), which have been demonstrated to create a convincing sensation of walking [23]. This effectiveness stems from studies in perception psychology revealing that visual input often overrides proprioception (sensing the body's position, movement, and actions) and vestibular sensations (related to balance and motion) when they conflict [24]. Essentially, humans excel at estimating their momentary direction of motion but struggle to perceive their exact paths of travel [25].

In VEs, this means users instinctively adjust for minor inconsistencies during locomotion, particularly when visual, proprioceptive, and vestibular cues differ. This enables imperceptible redirections using visual cues provided by VEs, a characteristic feature of RDW. RDW employs curvature gains (rotations of the virtual scene), translational gains (altering linear movements to change perceived distances traveled), and rotational gains (adding extra rotations to the user's existing rotation). Comprehensive discussions on the mathematical formulations of these gains, their perceptual thresholds, and experimental validations are available in prior studies [23], [26]. Notably, research indicates that VR users adjust their movement speeds in response to significant translational gains, even when these gains are not consciously perceivable.

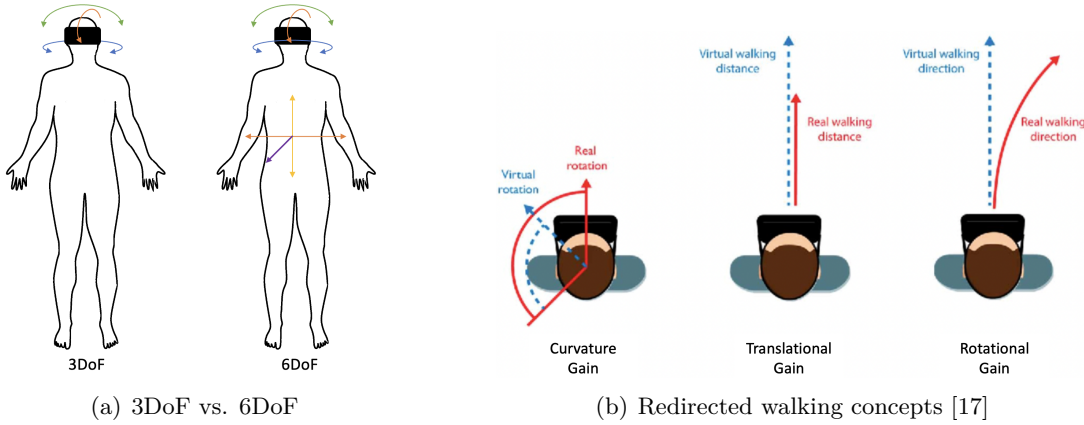


Figure 2: Main concepts of RDW enabled through non-tethered wireless HMDs [13]

2.2 Reconfigurable Intelligent Surfaces

RISs are envisioned to become a key enabling technology for next-generation mobile systems, such as beyond-5G/Sixth Generation (6G). A RIS consists of an array of sub-wavelength elements (nb., also known as unit cells) that can alter the Electromagnetic (EM) response of the impinging Radio-Frequency (RF) signals in a nearly passive way. Indeed, RISs can dynamically re-focus the received EM waves towards desired directions in space by suitably configuring the scattering properties of each element. This ability unlocks new possibilities and opens up a new paradigm of the wireless environment, which has been treated as an optimization constraint in conventional systems, but can now be considered as a variable to be optimized, creating the so-called Smart Radio Environment (SRE). For example, when an obstacle hinders the LoS between the transmitter and the receiver, a strategically deployed RIS can alleviate this problem via (passive) beamforming so as to effectively create a virtual LoS, which guarantees favorable signal propagation conditions. This can be achieved, for instance, by suitably designing the re-configurable phase shift provided by each element to receive wireless signals such that the reflected signals may interfere constructively towards the desired direction and destructively elsewhere.

Prior research has underscored the advantages of integrating RISs into traditional multi-user wireless communication frameworks [11], [27]–[29]. For instance, Chaccour *et al.* demonstrated that the RIS can enhance both the sum data-rate and the reliability of data transfer in VR contexts [28]. Jalali *et al.* delved into the RIS design for energy efficiency and admission control maximization for Internet of Things (IoT) users with short packet lengths [11]. Besser *et al.* introduced a

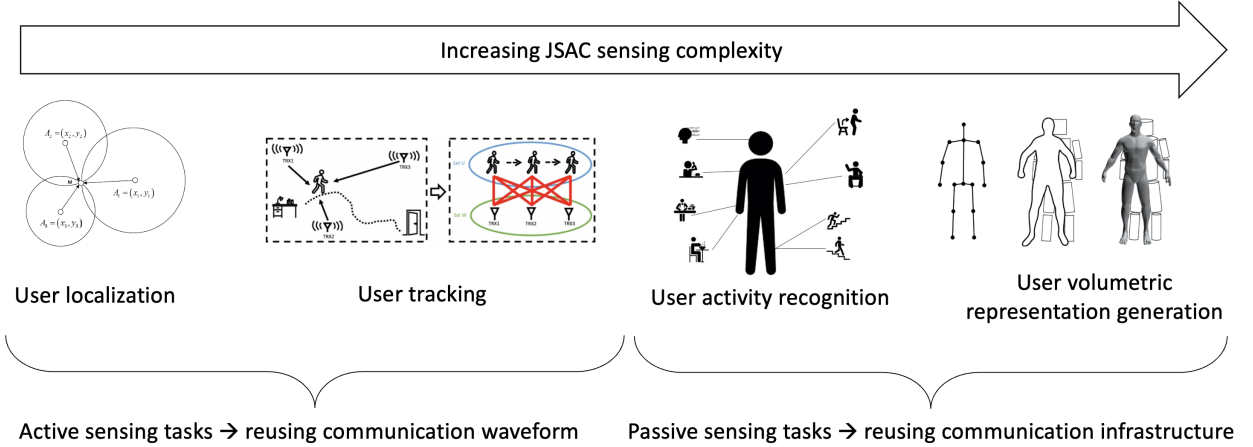


Figure 3: Example JCAS sensing tasks ordered by implementation complexity

phase hopping algorithm tailored for RIS-supported systems to elevate data transfer reliability without the necessity for Channel State Information (CSI) [27]. Furthermore, Zhou *et al.* studied a latency minimization problem for a multi-user secure RIS-aided VR delivery network with imperfect CSI [29].

Nonetheless, these studies have not explored the potential synergies of melding RIS with mmWave communication and sensing in a full-immersive multi-user VR scenario. Moreover, the incorporation of RISs in multi-user VR streaming systems, especially with optimal resource allocation, remains uncharted territory. Within RIS-enhanced VR streaming systems, the meticulous optimization of RIS phase shifts, placement, radiation patterns, and beamforming vectors stands vital to realizing high data rates. To the best of our knowledge, none of the research works have optimized the design of a RIS-assisted indoor VR network, where the RIS is considered to be deployed in a confined 3D space as a function of VR users' trajectory.

2.3 Real-Time Sensing for Enhanced Experiences

Furthermore, mmWave JCAS is a new paradigm gaining traction in the context of 6G. The general idea is for mmWave networks to support sensing in addition to supporting more traditional communication requirements. Integrated sensing can be performed with different aims, depending on the application scenario. For example, localization is one typical example of sensing in mmWave JCAS systems [30], which finds applications in e.g., vehicular networking scenarios [31]. More advanced applications can be found in the considered VR-specific scenario. Some examples include estimation of human pose or activities using mmWave signals [32], while more advanced ones envision full-body 3D representation capturing [33]. This advanced functionality is then envisioned to be used as a primer for generating interactive VEs with realistic 3D avatars prudently tracking users' movements.

While RIS was designed primarily for communication, the technology may bring significant benefits regarding performance, power consumption, and cost for localization and mapping, which is a promising function. As such, RIS-assisted JCAS systems have been extensively researched in various scenarios. Jiang *et al.* [34] investigate the joint design of transmit beamforming at the AP and reflection coefficients at the RIS to maximize the SNR of radar detection while meeting the communication need. The authors in [35] propose a two-dimensional hierarchical code book that simultaneously services the UE and locates the target using the RIS for positioning and communication. In [36], the authors propose a new Simultaneous (beam) Training and Sensing (STAS) protocol that utilizes downlink RIS beam scanning for concurrent training and sensing to achieve efficient RIS-aided mmWave JCAS. Finally, [37] proposes a JCAS system by introducing a RIS architecture to the communication system where location sensing and data transmission can be conducted simultaneously, occupying the same spectrum and time resources.

In general, channel parameters such as Time of Arrival (ToA)/Time Difference of Arrival (TDoA), Angle of Arrival (AoA), and Received Signal Strength (RSS) can be used for enabling the sensing tasks outlined in Figure 3. Taking user localization as an example, RSS-based localization

has poor location accuracy, which is influenced by network topology and propagation environment factors such as path loss exponent and shadowing effects. Although ToA/TDoA-based and AoA-based localization can achieve high location accuracy, they rely heavily on the LoS link, which can be disrupted, particularly in the mmWave case. As a result of its ability to establish a strong LoS path between the AP and the UE, the RIS has been proposed to overcome the blockage problem and improve location accuracy in the wireless communication system [37]. These properties, combined with their close relation to the environment's geometry and ability to be embedded in soft materials, as mentioned in [12], enable RIS to function as a "barrier" that defines the boundaries of the deployment environment and makes them desirable for mapping and localization purposes.

Toward enabling more advanced WiFi sensing tasks, approaches based of different types of radar imaging have been proposed. For example, in [38] the authors propose an imaging approach named 3D Reconstruction and Imaging via mmWave Radar (3DRIMR). 3DRIMR is a Generative Adversarial Network (GAN)-based deep learning architecture that reconstructs the 3D shape of an object in dense detailed point cloud format, based on sparse raw mmWave radar intensity data. The authors in [39], [40] enable the same 3D imaging functionality through the utilization if a Multiple-Input Multiple-Output (MIMO) radars combined with deep learning, Inverse Synthetic Aperture Radar (ISAR) imaging, and MIMO Frequency Modulated Continuous Wave (FMCW). These JCAS imaging approaches would inherently benefit for the significantly enhanced spatial distribution of communicating entities that the utilization of RISs would bring.

Toward the enablement of different types of passive sensing tasks, WiG [41] is highlighted as a pioneering low-cost gesture recognition system utilizing CSI extracted from WiFi signals. It achieves 92% accuracy in classifying gestures using an Support Vector Machine (SVM) classifier. Recent efforts in this domain emphasize robustness and generalization of CSI-based gesture recognition, as well as multi-person sensing. Efforts are also made in extending gesture recognition to multiple people simultaneously, as seen in WiMU [42], which recognizes up to 6 predefined gestures with high accuracy but lacks individual user identification. Recent attention has shifted towards mmWave signals for gesture recognition, as demonstrated by Ren's *et al.* [43] prototype utilizing 60 GHz mmWave technology. Their system achieves >95% accuracy using Range-Doppler Information (RDI) fed into a Convolutional Neural Network (CNN)+Long Short-Term Memory (LSTM) model for gesture recognition.

Deep learning approaches such as El [44] and CrossSense [45] aim for domain-independent activity recognition by extracting common features among different domains. Additionally, the focus is on cross-domain gesture recognition systems like [46] or WiPose [47], which constructs 3D human poses from WiFi signals, achieving 2.83 cm average error in localizing skeletal joints. Winect [48] is introduced as an environment-independent gesture recognition system capable of tracking free-form movements for human-computer interaction.

In the domain of generating user volumetric representations from JCAS imaging data, approaches such as Neural Radiance Fields (NeRF) [49] and Gaussian Splatting [50] are highly promising. However, their computational demands hinder real-time application viability. A practical approach for instantaneous VR user representation could involve body pose estimation from images, subsequently adjusting a pre-estimated 3D model of the user. Notably, body position prediction poses significant challenges due to the low resolution of images from mmWave transceivers.

It has been established in [7] that, in high-frequency communication, there is a direct link between sensing accuracy and SNR. When deploying a JCAS network, a single waveform transmits data and performs radar detection simultaneously. The waveform must be capable of accommodating radar detection requirements such as estimation accuracy. Range, speed, and communication requirements such as reliability, throughput, and latency necessitate a minimum SNR to function correctly, which is critical for reliable and accurate signal detection and interpretation. Hence, optimizing the sensing accuracy requires maintaining stable and high SNR across the deployment environment, which is addressed through the utilization of RISs.

3 Overcoming Communication and Sensing Challenges

3.1 Considered Scenario

The considered scenario is depicted in Figure 4. Specifically, an environment is considered in which the users are immersed in their VEs. The environment is constrained in its physical size as to provide a safe space for the users to immerse in their experiences. As such, the only potential collision perils for the users are other users and environmental boundaries. RDW is employed for directing the users primarily in a way that does not break their immersion, as discussed in Section 2. The users are immersed in VEs that are potentially unbound and interactive in the way that the action of one user affects the experience of the other, potentially collocated users. The perception of unbounded experiences are supported through RDW by introducing imperceivable rotational, translational, and curvature gains, as discussed previously.

In such a scenario, the goal is to provide the users with the consistently high throughput throughout their VEs. As such, the communication throughput between the AP and the users' HMD should be maximized, while simultaneously providing homogeneous coverage or minimizing the spatial variability of the throughput. This is of interest as it allows for downlink transmission of the video, audio, and tactile content toward the users' HMDs in a way that minimizes the jitter and allows for continuous delivery of equal-quality video frames. The fact that the users' VEs might be interactive poses an additional system requirement. Specifically, there is a need for capturing the actions of the users, as well as delivering the captured content to other users, where both actions should be carried out within the motion-to-photon latency for immersion maximization and avoiding motion sickness.

To support the outlined scenario's requirements, the utilization of high-frequency wireless networks operating in mmWave frequencies (i.e., 30-300 GHz) is often considered. This is because the delivery of VR content in real time, as well as real time sensing and distribution of users' actions to other users, requires significant communication bandwidth not present in traditional sub-6 GHz frequencies. In addition, large communication bandwidth available at such frequencies represents a primer for accurate network-supported sensing of users' actions, e.g., in the form of capturing the users' full 3D poses.

IEEE 802.11ay networks are a promising candidate for meeting the stringent requirements of the considered scenario. The IEEE 802.11ay standard envisions network operations at mmWave frequencies, which makes directional communication a feature allowing high speeds over short distances. This is achieved through advanced beamforming techniques, in which the AP and UEs can focus their transmissions in specific directions, improving signal strength and reliability. However, this directional nature of communication can create challenges in achieving uniform coverage within a given area [51]. The quality in the formation of beams varies with the number of antennas; as the number of antennas increases, the width of the beam is reduced, making the array more directional, thus improving beamforming. At the same time, as the number of antennas decreases, the beamforming declines [52]. When the number of antenna elements in a AP is limited, achieving uniform coverage over the entire area becomes difficult. This limitation can result in areas of weaker signal strength or coverage gaps, which can be particularly problematic for applications such as VR.

To counter these challenge, RISs are introduced to the considered full-immersive multiuser VR environments. Given that such environments will have to be safe spaces without collision hazards for the users apart from the environmental boundaries and other users [3], it is considered as a natural possibility to utilize RISs in the surrounding walls to support the communication and sensing challenges stemming from the scenario. RISs consist of large arrays of passive reflecting elements on a reconfigurable planar surface. These elements can independently modify the phase of an incoming signal before reflecting it towards its intended receiver. The integration of RIS can be a boon for users experiencing significant path loss, as the RIS creates additional propagation pathways – namely, reflected channels. Moreover, these RISs offer added degrees of freedom through the phase shifts of the reflective elements, which can be harnessed to minimize interference [11]. It is also worth noting that RISs are envisioned to be manufactures as passive, cheap, and flexible entities adaptable for indoor VR streaming setups, as they could be used as flexible environmental boundaries without collision hazard [12].

For the full-immersive VR scenario in Figure 4, a novel radio resource allocation optimization in a RIS-assisted mmWave network is studied, where a multi-antenna AP transmits information symbols to a set of single-antenna HMDs. In particular, a resource allocation algorithm is designed

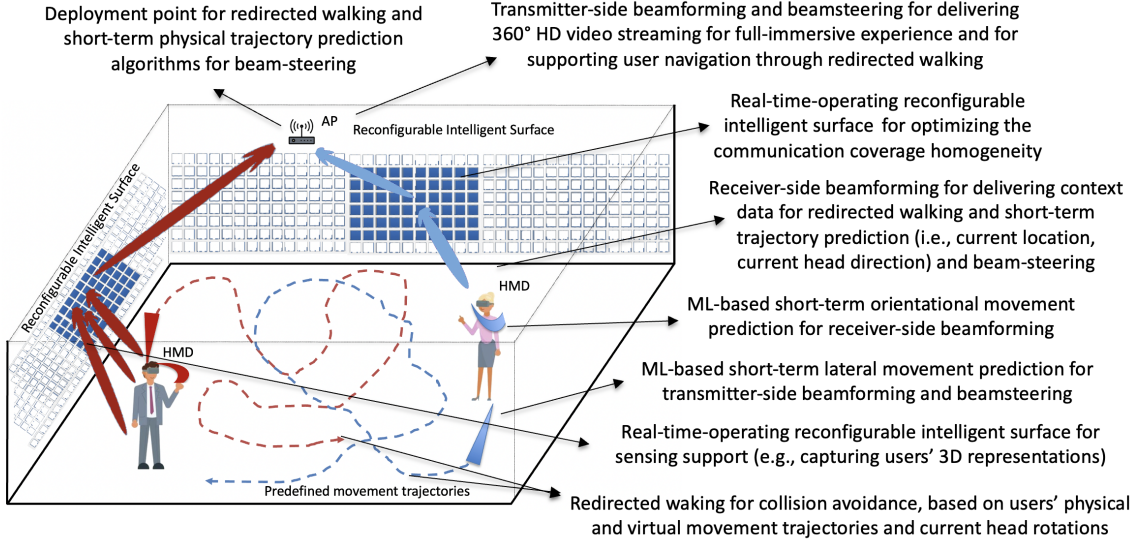


Figure 4: Considered full-immersive RIS-assisted mmWave scenario.

to maximize the system’s sum data-rate subject to peak transmit power feasibility and QoS constraints. The formulated problem is non-convex due to the high coupling of optimization variables. To tackle this, an AO algorithm is employed, segmenting the main optimization problem into four distinct sub-problems, in which each sub-problem is optimally solved.

3.2 Location-based RIS Resource Allocation for Communication and Sensing

As depicted in Figure 4, a wireless communication system is considered in which RISs are used to redirect data to a set of UEs attached to the users’ HMDs. The set of all UEs is represented as $\mathcal{K} = \{1, \dots, K\}$ and the set of RISs is represented as $\mathcal{I} = \{1, \dots, I\}$ with each element of a RIS being denoted by $\mathcal{M} = \{1, \dots, M\}$. In many real-world applications, utilizing RISs for wireless communication proves beneficial. For instance, in applications that can tolerate delays like periodic sensing data collection, using the RIS to sequentially communicate with UEs can be an economical choice. The goal is to fine tune the RISs element allocation to achieve maximum SNR over a fixed time span $T > 0$. As explained in Section 2, it is critical to maintain a high SNR to provide extensive and reliable coverage to deliver stronger signals, reduced dead zones and improved comprehensive data collection to enhance communication and sensing. The time duration T is partitioned into N uniformly spaced time intervals, given by $T = N\xi_t$. Specifically, ξ_t denotes the length of each individual time slot, and N is defined as the set of all these time slots, represented by $\mathcal{N} = \{1, \dots, N\}$.

In this context, a 3D Cartesian coordinate system is adopted, with the AP situated at a fixed location $\mathbf{a} = [a_x, a_y, a_z]^T \in \mathbb{R}^{3 \times 1}$. On the other hand, the UEs are placed in a ground location, and their trajectory follows the path $\mathbf{u}[n, k] = [u_x[n, k], u_y[n, k], u_z[n, k]]^T \in \mathbb{R}^{3 \times 1}$.

The location-based allocation of RISs elements is pivotal for signal redirection. When projected onto the vertical plane (e.g., on each wall of a room or office enforcement), the central location of i -th RIS element allocation is represented by $\mathbf{s}^i[n] = [s_x^i[n], s_y^i[n], s_z^i[n]]^T \in \mathbb{R}^{3 \times 1}$.

Furthermore, the area of interest is confined to \mathcal{I} half-spaces $\mathcal{D}_\infty = \{\mathcal{D}_1, \dots, \mathcal{D}_I\}$ where each RIS could potentially be placed. The central position of each RIS is strategically placed in any of these half-space regions to optimize signal quality, minimize interference, and enhance overall wireless communication system efficiency. This is done so long as no two RISs are placed in one half-space; that is, each RIS must be positioned in a different half-space. Within the first half-space, the first RIS can be strategically positioned and \mathcal{D}_1 is defined as:

$$\begin{aligned} x_{min}^i &< s_x^i[n] < x_{max}^i, \\ y_{min}^i &< s_y^i[n] < y_{max}^i, \\ z_{min}^i &< s_z^i[n] < z_{max}^i, \quad \forall n \in \mathcal{N}, \forall i \in \mathcal{I}. \end{aligned} \quad (1)$$

The domain in Equation (1) defines the first region, i.e., \mathcal{D}_1 , where the first RIS needs to be centrally positioned. Likewise, one can establish $\mathcal{D}_\infty/\mathcal{D}_1 = \{\mathcal{D}_2, \dots, \mathcal{D}_I\}$ to represent the regions within which the remaining RISs elements are allocated. These regions make sure that RISs elements are allocated in one of the corner walls of the environment, as depicted in Figure 4. In this configuration, the distance between the RIS and the UE, as well as between the RIS and the AP over time, has a direct influence on the channel quality. Consequently, determining the optimal allocation of the RIS elements becomes crucial.

To clarify the discussion, the assumption is that the communication link between the RIS and the UEs is largely governed by the LoS channel. In the context of the considered setup, it is important to highlight that the RIS-UE channel is more inclined to maintain a prominent LoS link than AP-UE channels. For this explanation, one can also assume that the AP-UE channel is entirely obstructed by other UEs that block the LoS between the AP and the UE. Exploring Non-Line-of-Sight (NLoS) and multi-path fading channels will be reserved for subsequent studies. Additionally, any Doppler effect caused by the UE's mobility is presumed to be fully compensated for.

To expedite the utilization of RIS-aided communication, the radiation pattern of the RIS is also accounted for, as explored in [53], namely:

$$F(\psi_{i,k}, \varphi_i) = \begin{cases} \cos^3(\psi_{i,k}), & \psi_{i,k} \in [0, \pi/2], \varphi_i \in [0, 2\pi], \\ 0, & \psi_{i,k} \in (\pi/2, \pi], \varphi_i \in [0, 2\pi], \end{cases} \quad (2)$$

where $\psi_{i,k}$ and φ_i represent the elevation and azimuth angles, respectively, from the RIS to the AP/UE link. It is worth pointing out that the radiation pattern of the RIS remains consistent across various azimuth angles. To streamline the discussion, the argument φ_i is excluded from the function $F(\psi_{i,k}, \varphi_i)$ in (2) in subsequent equations, using $F(\psi_{i,k})$ in place of $F(\psi_{i,k}, \varphi_i)$. Given these conditions, the dynamic channel between the AP and RIS, and between the RIS and the k -th UE adheres to the free-space path loss model, which can be detailed as:

$$\tilde{\mathbf{h}}_i = \mathbf{h}_i \sqrt{\beta_{i,0} F(\psi_{i,0})}, \quad \forall i \in \mathcal{I}, \quad (3)$$

$$\tilde{\mathbf{g}}_{i,k} = \mathbf{g}_{i,k} \sqrt{\beta_{i,k} F(\psi_{i,k})}, \quad \forall i \in \mathcal{I}, \forall k \in \mathcal{K}, \quad (4)$$

where $\beta_{i,0}$ and $\beta_{i,k}$ symbolize the path loss, while $\mathbf{h}_i \in \mathbb{C}^{M \times 1}$ and $\mathbf{g}_{i,k} \in \mathbb{C}^{M \times 1}$ stand for the small-scale fading of the links between the AP and RIS and between the RIS and the k -th UE, respectively. Notably, the small-scale fading remains static throughout each coherence interval. In contrast, the path loss undergoes changes but at a much slower rate. This perspective is justifiable when considering that the distances between the users, the AP, and the RIS are significantly larger than the separations between the RIS elements [54], [55]. In light of this, $\beta_{i,0}$ and $\beta_{i,k}$ can be delineated as:

$$\beta_{i,k'} = c_0 \|\mathbf{d}_{i,k'}[n]\|^{-\alpha_{i,k'}}, \quad \forall k' \in \mathcal{K} \cup \{0\}, \forall i \in \mathcal{I}, \forall n \in \mathcal{N}, \quad (5)$$

where c_0 is the reference path loss at a distance of meter. Moreover, $\alpha_{i,0}$ and $\alpha_{i,k}, \forall k \in \mathcal{K}$ are the path loss exponents of links between AP and IRS and the link between IRS and UE k , respectively [56]. Moreover, the distance vectors from the IRS to the AP and k -th UE are respectively given by:

$$\mathbf{d}_{i,0}[n] = \mathbf{s}^i[n] - \mathbf{a}[s_x^i[n] - a_x, s_y^i[n] - a_y, s_z^i[n] - a_z]^T, \\ \forall i \in \mathcal{I}, \forall n \in \mathcal{N}, \quad (6)$$

$$\mathbf{d}_{i,k}[n] = \mathbf{s}^i[n] - \mathbf{u}[n, k] = [s_x^i[n] - u_x[n, k], s_y^i[n] - u_y[n, k], \\ s_z^i[n] - u_z[n, k]]^T, \\ \forall k \in \mathcal{K}, \forall i \in \mathcal{I}, \forall n \in \mathcal{N}. \quad (7)$$

To sum it up, the mathematical representation for the received signal at the k -th UE is as follows:

$$y_k = \sum_{i \in \mathcal{I}} \sqrt{P_{\text{AP}}} \tilde{\mathbf{g}}_{i,k}^H \Theta_i \tilde{\mathbf{h}}_i + n_k, \forall k \in \mathcal{K}. \quad (8)$$

where P_{AP} is the AP transmit power and n_k is the Additive White Gaussian Noise (AWGN) at the k -th UE, which follows a complex normal distribution with mean 0 and variance σ_k^2 . The RIS phase shift matrix is represented by Θ_i and is defined as $\Theta_i \equiv \text{diag}(\theta_1, \theta_2, \dots, \theta_M)$. Here, $\theta_m \in \mathbb{C}$ characterizes the reflection coefficient of the m -th RIS element. Specifically, $\theta_m \equiv \varrho_m e^{j\vartheta_m}$, where ϱ_m lies within $[0, 1]$, capturing the reflection amplitude, and ϑ_m spanning $[0, 2\pi]$ depicts the phase shift of the m -th RIS element. Notably, the j in the exponent represents the imaginary unit. Ultimately, by assuming there is no multi-user interference, the SNR at the k -th UE can be represented as follows:

$$\gamma_{i,k}(P_{\text{AP}}, \Psi_i, \beta_i, \Theta_i) = \frac{P_{\text{AP}} \beta_{i,0} F(\psi_{i,0}) \beta_{i,k} F(\psi_{i,k}) \left| \mathbf{g}_{i,k}^H \Theta_i \mathbf{h}_i \right|^2}{\sigma_k^2}, \\ \forall k \in \mathcal{K}, \forall i \in \mathcal{I}, \quad (9)$$

where Ψ_i and β_i are the collection of ψ 's and β 's according to $\Psi_i \triangleq [\psi_{i,0}, \dots, \psi_{i,K}]$ and $\beta_i \triangleq [\beta_{i,0}, \dots, \beta_{i,K}]$, refer to the RIS location decision variables, $\mathbf{s}[n]$. Given the SNR expression as articulated above, in Equation (9), the Spectral Efficiency (SE) for the k -th UE, measured in [bit/s/Hz], can be expressed as:

$$R(P_{\text{AP}}, \Psi_i, \beta_i, \Theta_i) = \log_2 (1 + \gamma_{i,k}(P_{\text{AP}}, \Psi_i, \beta_i, \Theta_i)), \forall k \in \mathcal{K}, \quad (10)$$

consequently, the sum data-rate for all UEs can be written as:

$$R_{\text{tot}}(P_{\text{AP}}, \Psi_i, \beta_i, \Theta_i) = B \sum_{\forall k \in \mathcal{K}} R(P_{\text{AP}}, \Psi_i, \beta_i, \Theta_i), \quad (11)$$

where B represents the bandwidth of the network. In the context of this study, it is also of high importance to enhance the total data-rate. This can be achieved by fine-tuning parameters such as transmit power control, location-based allocation of RIS elements, and their corresponding phase shifts. With this objective in mind, the optimization problem can be formulated as:

$$P_1 : \max_{P_{\text{AP}}, \Psi_i, \beta_i, \Theta_i} R_{\text{tot}}(P_{\text{AP}}, \Psi_i, \beta_i, \Theta_i), \quad (12a)$$

$$\text{s.t. } P_{\text{AP}} \leq P_{\text{AP}}^{\max}, \quad (12b)$$

$$|\theta_m| \leq 1, \forall m \in \mathcal{M}, \quad (12c)$$

$$x_{\min}^i < s_x^i[n] < x_{\max}^i, \forall n \in \mathcal{N}, \forall i \in \mathcal{I}, \quad (12d)$$

$$y_{\min}^i < s_y^i[n] < y_{\max}^i, \forall n \in \mathcal{N}, \forall i \in \mathcal{I}, \quad (12e)$$

$$z_{\min}^i < s_z^i[n] < z_{\max}^i, \forall n \in \mathcal{N}, \forall i \in \mathcal{I}. \quad (12f)$$

Constraint (12b) ensures that the transmission power remains within the upper limits set for the AP. Constraint (12c) specifies the bounds within which the reflection coefficient for every RIS element must operate. Constraints (12d)-(12f) ensure the RIS is positioned in one of the corner

walls of the room. Given the presence of a non-concave objective function and the non-convex nature of constraint (12c), the optimization problem laid out in (12) is distinctly nonconvex. This inherent complexity makes it challenging to derive a straightforward solution for the problem. As a result, AO methods or approximations might be needed to address non-convexity effectively.

3.2.1 AP Transmit Power Control

First, Ψ_i , β_i , and Θ_i are fixed, and the optimization of P_{AP} is considered. Thus, the corresponding optimization problem of AP transmit power control [57] with a transformed objective function can then be formulated as follows:

$$P_2 : \max_{P_{\text{AP}}} \sum_{\forall k \in \mathcal{K}} \frac{P_{\text{AP}} \beta_{i,0} F(\psi_{i,0}) \beta_{i,k} F(\psi_{i,k}) |\mathbf{g}_k^H \Theta_i \mathbf{h}_i|^2}{\sigma_k^2}, \quad (13a)$$

$$\text{s.t. } P_{\text{AP}} \leq P_{\text{AP}}^{\max}. \quad (13b)$$

One can readily prove that the optimization problem (13) is affine and convex. Thus, one can exploit the properties of convex optimization to derive solutions. To do so, one approach is to differentiate the objective function concerning P_{AP} , the AP transmit power. By setting this first-order derivative to zero and taking into account the constraint that dictates the maximum transmit power, one can derive the optimal solution for the problem described in (13). This solution can be represented as $P_{\text{AP}} = \max \{0, P_{\text{AP}}^{\max}\}$.

3.2.2 Location-based Allocation of RIS Elements

In this subsection, a subproblem is formulated, wherein the RIS element allocation is optimized with a fixed RIS phase shift and radiation pattern, i.e., Ψ_i and Θ_i are known. Therefore, the optimization problem for the center position of RIS element allocation can be written as follows:

$$P_3 : \max_{\mathbf{s}[n]} \sum_{\forall k \in \mathcal{K}} \frac{c_0^2 F(\psi_{i,0}) F(\psi_{i,k}) |\mathbf{g}_k^H \Theta_i \mathbf{h}_i|^2}{\sigma_k^2 \|\mathbf{s}[n] - \mathbf{a}\|^{\alpha_0} \|\mathbf{s}[n] - \mathbf{u}[n, k]\|^{\alpha_k}}, \quad (14a)$$

$$\text{s.t. (12d) -- (12f)}, \quad (14b)$$

where β_i 's are replaced by the RIS' location decision variables, $\mathbf{s}[n]$. It can be seen optimization problem (14). Thus, an optimal solution can be found. By setting the first-order derivative of the objective function with respect to $\mathbf{s}[n]$ to zero and considering the maximum SNR, the following two qualities are obtained:

$$\begin{aligned} & \frac{(a_x - s_x[n])}{(a_x - s_x[n])^2 + (a_y - s_y^i[n])^2 + (a_z - s_z^i[n])^2} \\ &= \frac{(s_x^i[n] - u_y[n, k])}{(s_x^i[n] - u_y[n, k])^2 + (s_y^i[n] - u_y[n, k])^2 + (s_z^i[n] - u_z[n, k])^2}, \forall n \in \mathcal{N}, \forall k \in \mathcal{K}, \forall i \in \mathcal{I}, \end{aligned} \quad (15)$$

$$\begin{aligned} & \frac{(a_y - s_y^i[n])}{(a_x - s_x^i[n])^2 + (a_y - s_y^i[n])^2 + (a_z - s_z^i[n])^2} \\ &= \frac{(s_y^i[n] - u_y[n, k])}{(s_x^i[n] - u_y[n, k])^2 + (s_y^i[n] - u_y[n, k])^2 + (s_z^i[n] - u_z[n, k])^2}, \forall n \in \mathcal{N}, \forall k \in \mathcal{K}, \forall i \in \mathcal{I}, \end{aligned} \quad (16)$$

$$\begin{aligned} & \frac{(a_z - s_z^i[n])}{(a_x - s_x^i[n])^2 + (a_y - s_y^i[n])^2 + (a_z - s_z^i[n])^2} \\ &= \frac{(s_z^i[n] - u_z[n, k])}{(s_x^i[n] - u_z[n, k])^2 + (s_y^i[n] - u_z[n, k])^2 + (s_z^i[n] - u_z[n, k])^2}, \forall n \in \mathcal{N}, \forall k \in \mathcal{K}, \forall i \in \mathcal{I}, \end{aligned} \quad (17)$$

where it is assumed $\alpha_{i,k} = 2$ [58] in order to achieve closed-form solutions. Given the aforementioned inequalities, an iterative location-based approach is employed to determine the allocation of RIS elements. Starting with predetermined or initial values for $s_x^i[n]$, $s_y^i[n]$, and $s_z^i[n]$, the optimal x -coordinate, y -coordinate and z -coordinate of the RIS are computed using the equation referenced by (15)–(17) iteratively and following the constraints (12d)–(12f). This iterative refinement converges to optimize the RIS placement in the 3D plane based on the system's performance metric and constraints. The iterative algorithm is given in Algorithm 1.

Algorithm 1 Algorithm for Location-based Allocation of RIS Elements

Input: Initial parameters $s_x[n], s_y[n], s_z[n]$, maximum iterations Q (with q as the iteration index) and precision P

Output: Optimal parameters $s_x^i[n]^*, s_y^i[n]^*, s_z^i[n]^*$

- 1: **repeat**
- 2: $p_{s_x^i[n]} = s_x^i[n]$
- 3: $p_{s_y^i[n]} = s_y^i[n]$
- 4: $p_{s_z^i[n]} = s_z^i[n]$
- 5: Compute gradient vector for 15 $\nabla J(s_x^i[n])$
- 6: Compute gradient vector for 16 $\nabla J(s_y^i[n])$
- 7: Compute gradient vector for 17 $\nabla J(s_z^i[n])$
- 8: Update parameters: $s_x^i[n] \leftarrow s_x^i[n] + \alpha \cdot \nabla J(s_x^i[n])$
- 9: Update parameters: $s_y^i[n] \leftarrow s_y^i[n] + \alpha \cdot \nabla J(s_y^i[n])$
- 10: Update parameters: $s_z^i[n] \leftarrow s_z^i[n] + \alpha \cdot \nabla J(s_z^i[n])$
- 11: $p = \|s_x^i[n] - p_{s_x^i[n]}\| + \|s_y^i[n] - p_{s_y^i[n]}\| + \|s_z^i[n] - p_{s_z^i[n]}\|$
- 12: $q \leftarrow q + 1$
- 13: **until** $p < P$ and $q < Q$
- 14: **return** $s_x^i[n]^* = s_x^i[n], s_y^i[n]^* = s_y^i[n], s_z^i[n]^* = s_z^i[n]$

3.2.3 RIS Passive Beamforming and Radiation Pattern Optimization

The subproblem of jointly optimizing Ψ_i and Θ_i with fixed P_{AP} and β_i is considered here, which can be given by:

$$P_4 : \max_{\Psi_i, \Theta_i} R_{\text{tot}}(\Psi_i, \Theta_i), \quad (18a)$$

$$\text{s.t. } |\theta_m| \leq 1, \forall m \in \mathcal{M}. \quad (18b)$$

Unlike the preceding two subproblems that have closed-form solutions, obtaining a closed-form solution for Ψ_i and Θ_i is challenging due primarily to the constraints associated with the RIS unit modulus. Fortunately, one could utilize successive convex approximation methods to transform the rank unit modulo constraint into linear matrix inequalities per iteration based on [11]. The final iterative-based AO algorithm is provided in Algorithm 2.

3.3 Computational Complexity and Convergence Analysis

In this section, a comprehensive analysis of the computational complexity associated with the outlined algorithm is conducted, as referenced in [59]. This exploration is crucial for understanding the practical applicability and efficiency of the design resource allocation algorithm.

Initially, the optimization problem P_2 (13) is examined. This problem is distinguished by its convex nature, enabling efficient resolution within a polynomial time complexity order. Characterized by a singular optimization variable coupled with one convex constraint, the computational complexity for each iteration maintains a constant order, denoted as:

$$O_1 = \mathcal{O}(1). \quad (19)$$

Algorithm 2 Iterative AO Algorithm

Input: Set iteration number $e = 0$, maximum number of iterations E_{\max} , and initialize the coordinates $P_{\text{AP}} = P_{\text{AP}}^0$, $\Psi_e = \Psi_e^0$, $\beta_e = \beta_e^0$, $\Theta_e = \Theta_e^0$.

repeat

- 2: Solve Equation (13) for given $\{\Psi_i^{e-1}, \beta_i^{e-1}, \Theta_i^{e-1}\}$ and obtain the optimal P_{AP}^e .
- Solve Equation (14) for given $\{P_{\text{AP}}^{e-1}, \Psi_i^{e-1}, \Theta_i^{e-1}\}$ and obtain the optimal β_i^e .
- 4: Solve Equation (18) for given $\{P_{\text{AP}}^{e-1}, \beta_i^{e-1}\}$ and obtain the sub-optimal $\{\Psi_i^e, \Theta_i^e\}$.

until $e = E_{\max}$

6: **return** $\{P_{\text{AP}}^*, \Psi_i^*, \beta_i^*, \Theta_i^*\} = \{P_{\text{AP}}^e, \Psi_i^e, \beta_i^e, \Theta_i^e\}$

The optimization problem P_3 (14) is a convex problem of increased complexity, defined by $3IN$ decision variables and an equal number of constraints, reflecting a significant expansion in computational demands compared to P_2 (13). Consequently, the complexity for this segment is approximated as:

$$O_2 \approx \mathcal{O}((IN)^4), \quad (20)$$

indicating a quartic relationship with the product of the number of RISs I and the number of UEs N . This polynomial increase emphasizes the computational intensity required as the problem dimensions expand.

Further complexity unfolds with the reformulation of Equation P_4 (18) into a Semi-Definite Program (SDP). The computational intricacy of an SDP, featuring w SDP constraints and engaging a positive semi-definite matrix of dimensions $v \times v$ is given by:

$$O_3 = \mathcal{O}(\sqrt{v} \log(1/\zeta)(wv^3 + w^2v^2 + w^3)). \quad (21)$$

Here, $\zeta > 0$ epitomizes the precision of the solution, as expounded in [11]. This expression highlights the subtle trade-off between matrix size, constraint volume, and desired accuracy in shaping computational workload.

The overall complexity of the proposed algorithmic solution is thus a function of the complexities of solving optimization problems (13), (14), and (18). This yields an aggregate complexity of:

$$\mathcal{O}_{\text{tot}} = \mathcal{O}(e_{\text{iter}}(O_1 + O_2 + O_3)), \quad (22)$$

offering a comprehensive overview of the computational demands of the algorithm across all stages of optimization. The overall complexity in \mathcal{O}_{tot} is an order four polynomial, where e_{iter} signifies the iteration count necessary for the AO iterative algorithm to achieve convergence.

4 Context-Aware RIS Utilization Performance

4.1 Evaluation Setup

A simulation framework is utilized for assessing the performance of the AO algorithm in a RIS-assisted full-immersive VR-supporting mmWave network, accounting for the locations of the HMDs, the AP, and the RIS within a 3D setting. The allocation of RIS resources is considered within the environment's outer walls, excluding floor and ceiling. The AP is centered on the ceiling at 3 m height with the HMDs navigating in environments sized 10×10 , 15×15 , or 20×20 m^2 , reflecting future deployment site configurations [13].

The proposed AO algorithm is derived for a generic number of RIS elements, where the allocation of the number of such resources will depend on the communication data-rate requirements of the future VR systems. In the instantiation of the approach 200 such elements are considered, each of them sized $\lambda/5$ [60], [61]. The discrete-event network simulator (ns-3) is utilized, in particular its WiGig module, which facilitates the analysis of the IEEE 802.11ay protocol's performance [62]. Moreover, a mmWave propagation model was integrated into the existing ns-3 framework that models the presence of RISs on the signal propagation in the deployment environment. The summary of relevant simulation parameters is given in Table 1.

Two unbound VEs have been designed, as shown in Figure 5. In multiuser VR setups, three different types of user coexistence can be distinguished: i) the users sharing solely the tracking space, ii) the users sharing only the VE, iii) the users sharing both the tracking space and VEs. In this study, both of the designed experiences abide to the first category. In the “straight path” experience, the users are assumed to follow a straight path during the full duration of the VE. This was considered as the worst case scenario given that the RDW algorithm was intuitively expected to have the most difficulties to unnoticeably redirect the users. In the “random path” experience, the users are assumed to immerse in an unbound VE and follow a randomly curved path. Hence, the curvature introduced by the RDW algorithm was expected to be less noticeable. Conceptually, the experiments consisted of the users walking in the unbound VEs while being confined to the restricted tracking space. The positional data of the users was utilized by the RDW algorithm to steer them inside the confined physical environment for collision avoidance. The physical walking trajectories for the two considered scenarios were generated utilizing the simulator from [63].

In the evaluation of communication and active sensing tasks, the optimization aim is to maximize the communication throughput, while simultaneously maintaining stable SNR for optimizing the active sensing tasks of the network. First, in the “*NorIS*” approach, the LoS path from the AP to the HMD is examined. This approach is considered as a baseline for demonstrating the benefits of utilizing the RISs. Moreover, the proposed “*Optimal*” approach follows Algorithm 2 for dynamically adjusting the RIS configuration and resources allocation based on the HMD, AP, and RIS locations, and RIS radiation patterns. The RIS element allocation at a “*Random*” location is further considered, as well as at an “*Oracle*” location. These approaches are also considered as baselines, however to demonstrate the benefits of the proposed location-based allocation and the achievable performance of optimal RIS element allocation, respectively. The oracle location for the RIS element allocation is identified by considering all potential locations across room walls, assuming 0.1 m-sized spacing between neighbouring locations, and selecting the one that maximizes the SNR of the AP-RIS-HMD link. This approach is considered as an optimal approach, however at the cost of non-real-time operation. Besides, the “*Best path*” is used to demonstrate the performance of the combination of either the direct AP-HMD and AP-RIS-HMD links or RIS elements allocated utilizing the “*Optimal*” approach, with the criterion being the SNR maximization.

The modelling of passive sensing tasks is based on finding the UE's 3D imaging reconstruction and location by combining mmWave FMCW signals with RIS positioning. FMCW signals exhibit a linear frequency change over time and can be mathematically described as:

$$m(t) = \cos \left(2\pi \left(f_{ct} + \frac{1}{2} Kt^2 \right) \right), \quad 0 \leq t \leq T, \quad (23)$$

where f_c denotes the carrier frequency and $K = \frac{B}{T}$ represents the frequency slope. By leveraging the linear increase in frequency and the concept that time delay results in frequency shift, the Time of Flight (ToF) (τ) can be estimated for computing the distance to the target as

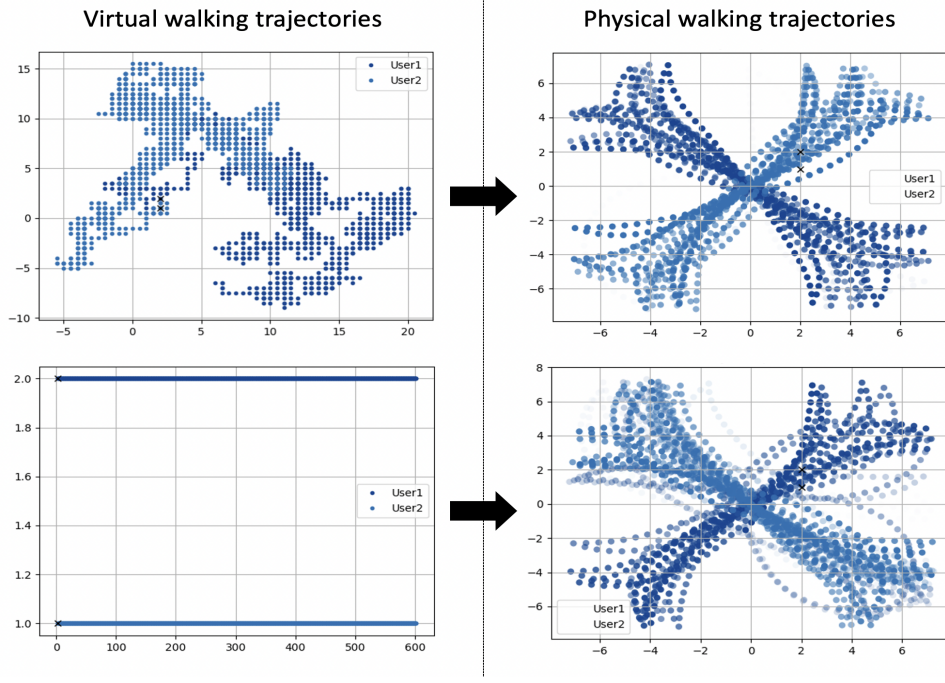


Figure 5: Physical and virtual path of two users immersed in random and straight VEs

Table 1: Baseline simulation parameters for communication and active sensing tasks

Parameter Name	Parameter Value
Application Type	OnOffApplication
Data Rate	150 Mbps
Flow Direction	Downlink
Payload Size	1448 Bytes
Transport Protocol	UDP
MAC Queue Size	4000 Packets
Aggregation Type	A-MSDU and A-MPDU
MAC / PHY	CSMA/CA / SC DMG MCS-10
Transmit Power / Sectors	10 mW / 8
Rx Noise Figure	10 dB
Operating Frequency	60.48 GHz

$\tau = \frac{d_t(x,y,z) + d_{ri}(x,y,z)}{c}$. Taking into account the target reflectivity and round-trip decay, the received signal at the i^{th} receiver can be expressed as:

$$Sb_i(x, y, z, t) = \alpha_i e^{j2\pi \frac{Kd_i(x,y,z)}{c}t}, \quad (24)$$

$$\alpha_i = \sigma_0 i e^{j2\pi f_c \tau_i} \quad (25)$$

where α_i represents the attenuated amplitude from the i^{th} receiver in relation to the specified target, taking into account the distance and target reflectivity which in the evaluation setup is 0. It also contains the phase shift of the central frequency term.

The objective of the passive sensing tasks of the network is to reconstruct the user's volumetric representation, for which a single target or point reflector is insufficient. Therefore, the formulation is expanded to account for multiple targets. The total received signal at the i^{th} receiver can be expressed as:

$$St_i(t) = \sum_{l=1}^L \alpha_{il} e^{j2\pi K \tau_{li} t} \quad (26)$$

Table 2: Baseline simulation parameters for advanced sensing tasks

Parameter Name	Parameter Value
Transmit Power	10 mW
Rx Noise Figure	10 dB
Operating Frequency	60.48 GHz
Bandwidth	1.2 GHz
FMCW Sweep Time	0.8 ms
Sampling Rate	500 kHz
Number of RIS Elements	400

where L represents the number of targets, that will depend on the reflectivity of the points and their occlusion. Additional sensing-related simulation parameters are outlined in Table 2.

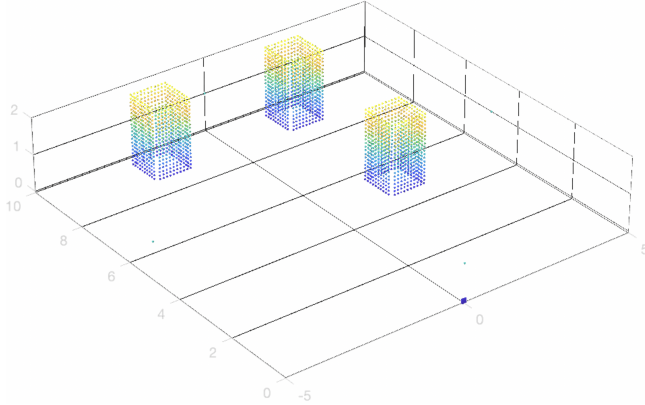


Figure 6: Model for advanced passive sensing of users' volumetric representations

To perform an exhaustive analysis and compare the homogeneity of the signal's SNR averaged over different UE locations, it is assumed that the VR users can be modeled as a box (cf., Figure 6). Four algorithms are considered for delivering sensing signals to the users (i.e., boxes) in a way that minimizes the spatial variability of SNR across the box walls, as such delivery homogenizes the quality of advanced sensing across the entire target, which is of importance for immersion maximization. First, in the "*NoRIS*" approach only LoS signals from the AP are considered. Moreover, in the "*Random*" approach the allocation of RIS elements is performed at a random position along each outer wall of the environment. Additionally, the "*Exhaustive Search*" approach seeks the optimal coordinates for the RIS element allocation exhaustively and is considered as an oracle approach due to the infeasibility of its real-time operation. Finally, the module has an "*Optimal*" approach, which is able to find a sub-optimal RIS element allocation based on the outlined AO approach, and features real-time operation.

4.2 Evaluation Results

4.2.1 Communication and Active Sensing Coverage, and Active Sensing Accuracy

The communication coverage of different approaches is expressed through average throughput and its standard deviation against a maximum threshold of 150 Mbps, focusing on scenarios with a single and multiple HMDs navigating through different environments (cf., Table 3). A snapshot of the results, focusing on the $15 \times 15 \text{ m}^2$ environment, is depicted in Figure 7. The throughput in each environment peaks when the RIS is optimally positioned for each HMD, in comparison to scenarios without the RIS and with its resource allocation at a random location. RIS resource allocation at an oracle location occasionally yields higher throughput, yet the AO algorithm can closely match its performance for the majority of HMD locations, despite its real-time-operating nature. Notably, the average throughput considering both the optimal RIS path and the direct HMD-AP channel is

Table 3: Summary of achieved results

Approach	Room size [m]	Avg [Mbps]	SD [Mbps]
No RIS	10×10	124, 08	68, 4051
	15×15	112, 25	74, 7407
	20×20	98, 063	79, 2939
Random	10×10	131, 97	60, 4667
	15×15	117, 58	62, 8617
	20×20	109, 40	67, 1633
Optimal	10×10	144, 97	50, 5537
	15×15	125, 10	68, 5524
	20×20	115, 87	72, 2035
Oracle	10×10	147, 89	40, 4191
	15×15	129, 34	47, 5146
	20×20	118, 74	49, 0862
LoS + RIS optimal	10×10	148, 90	39, 1131
	15×15	131, 34	46, 5221
	20×20	120, 73	48, 9770

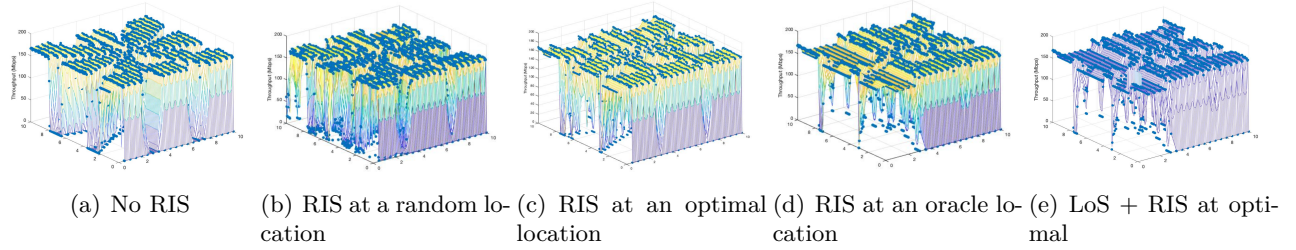


Figure 7: Communication coverage achieved by different approaches

highly comparable to the oracle. Analyzing standard deviation, performance of the network without the RIS shows higher throughput variability across environments compared to the scenarios with RIS support, even for its random resource allocation in the environment. Moreover, the “Optimal” location-based RIS resource allocation yielded by the AO approach, as well as its combination with LoS communication, offer consistent throughput and low SNR variability, even in multiuser scenarios (cf., Figure 8).

4.2.2 Advanced Sensing Accuracy

Table 4 presents the overall performance achieved in four specified scenarios, considering three different sizes of the deployment environment, and varying number of users. The data summarizes the scenario, number of users, average per-user SNR and for all users, as well as Standard Deviations (SDs) of the reported SNRs. The optimal placement of the RIS significantly influences both the average SD and the standard deviation of the averaged SNR for each UE. In comparison to the “NoRIS” and “Random” approaches, the exhaustive and optimal cases demonstrate substantially lower values for these metrics. For instance, in a 10×10 m² environment the average SD ranges from 0.294 to 0.371 dB in the “NoRIS” and “Random” approaches, while in the “Exhaustive” and “Optimal” ones it hovers around 0.2 and 0.25 dB, respectively. A more pronounced contrast emerges when examining the SD of the average SNR (i.e., SD SNR). In the “NoRIS” and “Random” approaches, this value is approximately 0.7 and 0.25 dB, whereas in the “Exhaustive” and “Optimal” ones it amounts to 0.05 and 0.11 dB, respectively.

The optimization of homogeneity has a trade-off in terms of the loss in SNR, as visible in Figure 9. This reduction in SNR during exhaustive search and optimal placement can be attributed to the fact that RIS element allocation should adapt to the environmental wall with the smallest

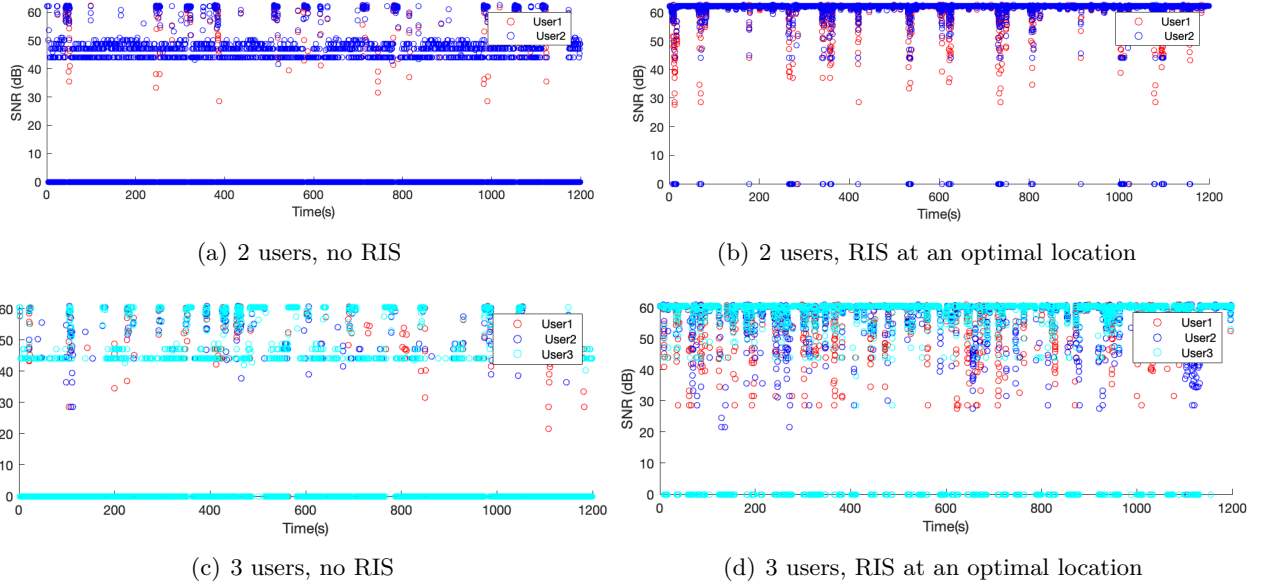


Figure 8: SNR enhancements due to RIS element allocation as yielded by the AO approach

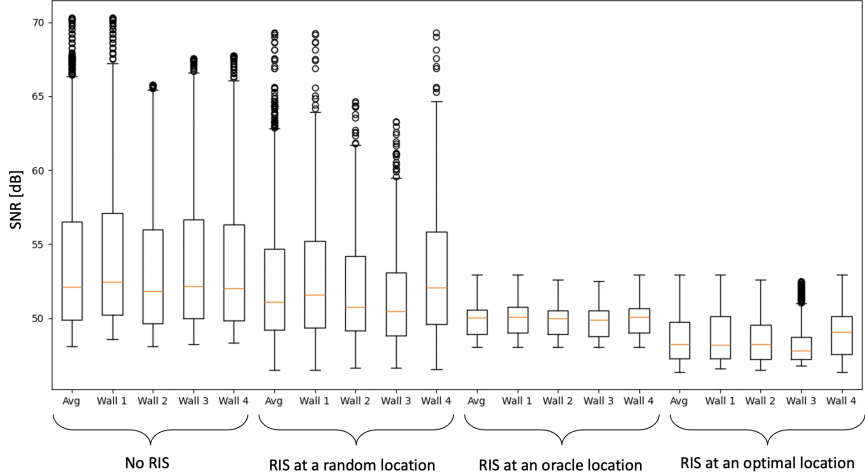


Figure 9: SNR distributions of different approaches in a $10 \times 10 \text{ m}^2$ environment

SNR, sacrificing the increase SNRs from other walls. Despite this, the decrease in SNR is needed in order to minimise the SD. The higher standard deviations imply increased fluctuations and it is indicative of lower reliability and QoS fluctuations.

Figure 9 illustrates the boxplots of SNR values within the confines of a $10 \times 10 \text{ m}^2$ environment. The initial five boxplots correspond to the “NoRIS” approach, with the first one representing the averaged SNR for the four walls. Subsequently, the following four boxplots depict the SNR for each wall of the UE model. It is evident that the data variability in the first two scenarios is significantly higher, indicating less homogeneity. In contrast, the “Optimal” and “Exhaustive” approaches showcase lower variability, with data appearing more compact. Although the SNR is slightly lower in these cases compared to the former, the trade-off becomes apparent in the low variability of data. The “Exhaustive” approach is an oracle that expectedly yields superior SNR and variability compared to the “Optimal” one, albeit at the expense of more than 15 times longer runtime without employing data parallelization.

Table 4: Achieved performance of different resource allocation approaches in differing sizes of the deployment environment and varying number of VR users

		10x10			15x15			20x20					
RIS	U	SNRu	SNRt	Avg	SD	SNRu	SNRt	Avg	SD	SNRu	SNRt	Avg	SD
No RIS	1	58,415	58,415	0,283	0,697	54,306	54,306	0,171	0,451	53,415	53,415	0,197	0,488
	2	58,438	58,623	0,287	0,717	54,306	55,088	0,171	0,451	53,697	53,514	0,197	0,488
	3	58,438	58,587	0,287	0,717	54,306	54,741	0,178	0,451	53,697	53,202	0,197	0,462
	58,809	0,324	0,696	55,869	55,869	0,247	0,247	0,586	53,331	0,165	0,165	0,462	0,488
	58,515	0,294	0,675	54,048	54,048	0,165	0,441	51,537	51,537	0,148	0,148	0,373	0,373
	58,198	58,198	0,331	0,2671	54,571	54,571	0,201	0,649	51,998	51,998	0,135	0,656	0,656
Random	2	58,201	58,209	0,318	0,241	54,674	54,691	0,207	0,505	52,031	52,048	0,137	0,667
	58,218	0,344	0,341	54,707	54,707	0,214	0,214	0,267	52,067	52,067	0,131	0,801	0,801
	3	58,137	58,235	0,321	0,171	54,674	54,718	0,206	0,49	52,009	51,853	0,136	0,595
	58,401	0,371	0,309	54,826	54,826	0,233	0,233	0,384	52,012	52,012	0,129	0,693	0,693
	58,166	0,332	0,317	54,654	54,654	0,203	0,203	0,883	51,537	51,537	0,132	0,199	0,199
	56,505	56,505	0,206	0,091	52,688	52,688	0,138	0,211	49,859	49,859	0,102	0,125	0,125
Exhaustive	2	56,564	56,492	0,197	0,0185	52,688	52,438	0,138	0,211	49,864	49,915	0,1102	0,125
	56,421	0,202	0,065	52,188	52,188	0,144	0,144	0,108	50,005	50,005	0,103	0,193	0,193
	3	56,564	56,503	0,197	0,021	52,688	52,515	0,131	0,211	49,825	49,922	0,102	0,125
	56,421	0,202	0,065	52,188	52,188	0,144	0,144	0,108	53,005	53,005	0,103	0,193	0,193
	56,525	0,213	0,117	52,668	52,668	0,132	0,132	0,036	49,935	49,935	0,094	0,117	0,117
	54,866	54,866	0,253	0,113	51,213	51,213	0,166	0,289	48,63	48,63	0,125	0,261	0,261
Optimal	2	55,534	55,049	0,244	0,118	51,772	51,409	0,165	0,241	48,803	48,781	0,124	0,266
	54,561	0,254	0,108	51,046	51,046	0,166	0,166	0,225	48,756	48,756	0,126	0,243	0,243
	3	55,534	55,049	0,244	0,118	51,772	51,251	0,165	0,241	48,803	48,717	0,124	0,266
	54,561	0,254	0,108	51,046	51,061	0,195	0,195	0,225	48,756	48,756	0,126	0,243	0,243
		55,341	0,263	0,195	51,061	0,163	0,276	0,276	48,592	48,592	0,124	0,301	0,301

5 Conclusions and Implications

This Chapter advocates for the utilization of Reconfigurable Intelligent Surfaces (RISs) as an integral part of millimeter Wave (mmWave)-supported full-immersive multiuser Virtual Reality (VR) setups. The utilization of RISs is envisaged for the enablement of communication (e.g., Non-Line-of-Sight (NLoS) avoidance), active sensing (e.g., support for user localization), and passive sensing tasks (e.g., user pose estimation or generation of full volumetric representations). In general, additional spatial diversity and degree of freedom introduced by RISs yield intuitive benefits to all these tasks, while system-level RISs optimization can further accentuate the benefits.

In that regard, a low-complexity Alternative Optimization (AO) algorithm for RIS resource allocation has been presented. The algorithm calculates the optimal placement of the centre position of RIS element allocation as a function of context-awareness, i.e., the User Equipments (UEs) and Access Point (AP) locations in the deployment environment. The proposed approach was evaluated in simulation, illustrating the advantages of utilizing the RISs in future fully-immersed VR environments and the efficacy of the approach. Future efforts should consist of system-level prototypical implementations and experimental performance characterizations of the proposed system.

Appendix

In the following, we prove that the proposed AO algorithm is convergent.

Proposition 1 *The objective function value of P_1 would be improved via this iterative algorithm.*

Proof 1 Let us consider $\{P_{\text{AP}}^{(j)}, \Psi_i^{(j)}, \beta_i^{(j+1)}, \Theta_i^{(j+1)}\}$ as the feasible solution set to P_4 . Then, the feasible solution set of P_4 is a feasible solution to P_1 as well. Therefore, $\{P_{\text{AP}}^{(j)}, \Psi_i^{(j)}, \beta_i^{(j)}, \Theta_i^{(j)}\}$ and $\{P_{\text{AP}}^{(j+1)}, \Psi_i^{(j+1)}, \beta_i^{(j)}, \Theta_i^{(j)}\}$ are feasible to P_1 in the (j) -th and $(j+1)$ -th iterations, respectively. Now, we define $f_{P_1}(P_{\text{AP}}^{(j)}, \Psi_i^{(j)}, \beta_i^{(j)}, \Theta_i^{(j)})$, $f_{P_4}(\beta_i^{(j)}, \Theta_i^{(j)})$, $f_{P_3}(\Psi_i^{(j)})$, and $f_{P_2}(P_{\text{AP}}^{(j)})$ as the objective functions of problem P_1 , P_4 and P_2 in the (j) -th iteration, respectively. Thus, we have

$$\begin{aligned} & f_{P_1}(P_{\text{AP}}^{(j+1)}, \Psi_i^{(j+1)}, \beta_i^{(j+1)}, \Theta_i^{(j+1)}) \\ & \stackrel{(a)}{=} f_{P_4}(\beta_i^{(j+1)}, \Theta_i^{(j+1)}) \stackrel{(b)}{\geq} f_{P_4}(\beta_i^{(j)}, \Theta_i^{(j)}) \\ & = f_{P_1}(P_{\text{AP}}^{(j)}, \Psi_i^{(j)}, \beta_i^{(j)}, \Theta_i^{(j)}), \end{aligned} \quad (27)$$

where (a) follows the fact that problem P_1 is equivalent to problem P_4 for optimal P_{AP} and Ψ_i , and (b) holds since $f_{P_4}(\beta_i^{(j+1)}, \Theta_i^{(j+1)}) \geq f_{P_4}(\beta_i^{(j)}, \Theta_i^{(j)})$ according to sub-problem 3 (that is, optimizing passive beamforming and radiation pattern optimization at the RIS). Similarly, for a given $P_{\text{AP}}^{(j)}, \beta_i^{(j)}, \Theta_i^{(j)}$, we have

$$\begin{aligned} & f_{P_1}(P_{\text{AP}}^{(j+1)}, \Psi_i^{(j+1)}, \beta_i^{(j+1)}, \Theta_i^{(j+1)}) \\ & \stackrel{(a)}{=} f_{P_3}(\Psi_i^{(j+1)}) \stackrel{(b)}{\geq} f_{P_3}(\Psi_i^{(j)}) \\ & = f_{P_1}(P_{\text{AP}}^{(j)}, \Psi_i^{(j)}, \beta_i^{(j)}, \Theta_i^{(j)}). \end{aligned} \quad (28)$$

where (a) follows the fact that problem P_1 is equivalent to problem P_3 for optimal P_{AP}, β_i , and Θ_i , and (b) holds since $f_{P_3}(\Psi_i^{(j+1)}) \geq f_{P_3}(\Psi_i^{(j)})$ according to sub-problem 2 (that is, the RIS optimal placement). Equivalently, for a given $\Psi_i^{(j)}, \beta_i^{(j)}, \Theta_i^{(j)}$, we have

$$\begin{aligned} & f_{P_1}(P_{\text{AP}}^{(j+1)}, \Psi_i^{(j+1)}, \beta_i^{(j+1)}, \Theta_i^{(j+1)}) \\ & \stackrel{(a)}{=} f_{P_2}(P_{\text{AP}}^{(j+1)}) \stackrel{(b)}{\geq} f_{P_2}(P_{\text{AP}}^{(j)}) \\ & = f_{P_1}(P_{\text{AP}}^{(j)}, \Psi_i^{(j)}, \beta_i^{(j)}, \Theta_i^{(j)}). \end{aligned} \quad (29)$$

where (a) follows the fact that problem P_1 is equivalent to problem P_2 for optimal Ψ_i, β_i , and Θ_i , and (b) holds since $f_{P_2}(P_{\text{AP}}^{(j+1)}) \geq f_{P_2}(P_{\text{AP}}^{(j)})$ according to sub-problem 1 (that is, the AP transmit power control). From the above three inequalities, we can conclude the following inequality holds

$$f_{P_1}(P_{\text{AP}}^{(j+1)}, \Psi_i^{(j+1)}, \beta_i^{(j+1)}, \Theta_i^{(j+1)}) \geq f_{P_1}(P_{\text{AP}}^{(j)}, \Psi_i^{(j)}, \beta_i^{(j)}, \Theta_i^{(j)}). \quad (30)$$

Thus, we have shown that the objective function of P_1 is monotonically non-decreasing after each iteration. \blacksquare

Acknowledgements

This work was supported by the Spanish Ministry of Economic Affairs and Digital Transformation and the European Union – NextGeneration EU, in the framework of the Recovery Plan, Transformation and Resilience (Call UNICO I+D 5G 2021, ref. number TSI-063000-2021-7); the European Union’s Horizon Europe’s research and innovation programme under grant agreement nº 101139161 — INSTINCT project; and MCIN / AEI / 10.13039 / 501100011033 / FEDER / UE HoloMit 2.0 project (nr. PID2021-126551OB-C21). This work was partially supported by the CHIST-ERA SAMBAS project (CHIST-ERA-20-SICT-003), with FWO (V478223N), ANR, NKFIH, and UKRI funding, and by the FWO WaveVR project (G034322N).

References

- [1] L. Muñoz-Saavedra, L. Miró-Amarante, and M. Domínguez-Morales, “Augmented and virtual reality evolution and future tendency,” *Applied Sciences*, vol. 10, no. 1, p. 322, 2020.
- [2] M. Chen, W. Saad, and C. Yin, “Virtual reality over wireless networks: Quality-of-service model and learning-based resource management,” *IEEE Transactions on Communications*, vol. 66, no. 11, pp. 5621–5635, 2018.
- [3] E. R. Bachmann, E. Hodgson, C. Hoffbauer, and J. Messinger, “Multi-user redirected walking and resetting using artificial potential fields,” *IEEE transactions on visualization and computer graphics*, vol. 25, no. 5, pp. 2022–2031, 2019.
- [4] F. Lemic, J. Struye, T. Van Onsem, J. Famaey, and X. C. Perez, “Predictive context-awareness for full-immersive multiuser virtual reality with redirected walking,” *IEEE Communications Magazine*, vol. 61, no. 9, pp. 32–38, 2023.
- [5] J. Struye, F. Lemic, and J. Famaey, “Coverage: Millimeter-wave beamforming for mobile interactive virtual reality,” *IEEE Transactions on Wireless Communications*, 2022.
- [6] D. Mehta, S. Sridhar, O. Sotnychenko, H. Rhodin, M. Shafiei, H.-P. Seidel, W. Xu, D. Casas, and C. Theobalt, “Vnect: Real-time 3d human pose estimation with a single rgb camera,” *Acm transactions on graphics (tog)*, vol. 36, no. 4, pp. 1–14, 2017.
- [7] Y. Wu, F. Lemic, C. Han, and Z. Chen, “Sensing integrated dft-spread ofdm waveform and deep learning-powered receiver design for terahertz integrated sensing and communication systems,” *IEEE Transactions on Communications*, vol. 71, no. 1, pp. 595–610, 2022.
- [8] P. Zhao, C. X. Lu, B. Wang, N. Trigoni, and A. Markham, “Cubelearn: End-to-end learning for human motion recognition from raw mmwave radar signals,” *IEEE Internet of Things Journal*, 2023.
- [9] P. Wang, J. Fang, X. Yuan, Z. Chen, and H. Li, “Intelligent reflecting surface-assisted millimeter wave communications: Joint active and passive precoding design,” *IEEE Transactions on Vehicular Technology*, vol. 69, no. 12, pp. 14 960–14 973, 2020.
- [10] Q. Wu and R. Zhang, “Intelligent reflecting surface enhanced wireless network via joint active and passive beamforming,” *IEEE Transactions on Wireless Communications*, vol. 18, no. 11, pp. 5394–5409, 2019.
- [11] J. Jalali, A. Khalili, A. Rezaei, R. Berkvens, M. Weyn, and J. Famaey, “Irs-based energy efficiency and admission control maximization for iot users with short packet lengths,” *IEEE Transactions on Vehicular Technology*, vol. 72, no. 9, pp. 12 379–12 384, 2023.

- [12] F. Lemic, S. Abadal, C. Han, J. M. Marquez-Barja, E. Alarcon, and J. Famaey, “Localization in power-constrained terahertz-operating software-defined metamaterials,” *Nano Communication Networks*, vol. 30, p. 100365, 2021.
- [13] T. Van Onsem, J. Struye, X. C. Perez, J. Famaey, and F. Lemic, “Toward full-immersive multiuser virtual reality with redirected walking,” *IEEE Access*, vol. 11, pp. 24722–24736, 2023.
- [14] M. S. Elbamby, C. Perfecto, M. Bennis, and K. Doppler, “Toward low-latency and ultra-reliable virtual reality,” *IEEE Network*, vol. 32, no. 2, pp. 78–84, 2018.
- [15] T. Nitsche, C. Cordeiro, A. B. Flores, E. W. Knightly, E. Perahia, and J. C. Widmer, “Ieee 802.11ad: Directional 60 ghz communication for multi-gigabit-per-second wi-fi,” *IEEE Communications Magazine*, vol. 52, no. 12, pp. 132–141, 2014.
- [16] Y. Wang, T. Zhang, S. Mao, and T. T. S. Rappaport, “Directional neighbor discovery in mmwave wireless networks,” *Digital Communications and Networks*, vol. 7, no. 1, pp. 1–15, 2021, ISSN: 2352-8648.
- [17] N. C. Nilsson, T. Peck, G. Bruder, E. Hodgson, S. Serafin, M. Whitton, F. Steinicke, and E. S. Rosenberg, “15 years of research on redirected walking in immersive virtual environments,” *IEEE computer graphics and applications*, vol. 38, no. 2, pp. 44–56, 2018.
- [18] F. Lemic, J. Struye, and J. Famaey, “Short-term trajectory prediction for full-immersive multiuser virtual reality with redirected walking,” in *GLOBECOM 2022-2022 IEEE Global Communications Conference*, IEEE, 2022, pp. 6139–6145.
- [19] J. Struye, F. Lemic, and J. Famaey, “Generating realistic synthetic head rotation data for extended reality using deep learning,” in *Proceedings of the 1st Workshop on Interactive eXtended Reality*, 2022, pp. 19–28.
- [20] A. Zhou, L. Wu, S. Xu, H. Ma, T. Wei, and X. Zhang, “Following the shadow: Agile 3-d beam-steering for 60 ghz wireless networks,” in *IEEE INFOCOM 2018 - IEEE Conference on Computer Communications*, 2018, pp. 2375–2383.
- [21] O. Abari, D. Bharadia, A. Duffield, and D. Katabi, “Enabling {high-quality} untethered virtual reality,” in *14th USENIX Symposium on Networked Systems Design and Implementation (NSDI 17)*, 2017, pp. 531–544.
- [22] J. Feasel, M. C. Whitton, and J. D. Wendt, “Llcm-wip: Low-latency, continuous-motion walking-in-place,” in *2008 IEEE symposium on 3D user interfaces*, IEEE, 2008, pp. 97–104.
- [23] F. Steinicke, G. Bruder, J. Jerald, H. Frenz, and M. Lappe, “Estimation of detection thresholds for redirected walking techniques,” *IEEE transactions on visualization and computer graphics*, vol. 16, no. 1, pp. 17–27, 2009.
- [24] J. Dichgans and T. Brandt, “Visual-vestibular interaction: Effects on self-motion perception and postural control,” in *Perception*, Springer, 1978, pp. 755–804.
- [25] M. Lappe, F. Bremmer, and A. V. van den Berg, “Perception of self-motion from visual flow,” *Trends in cognitive sciences*, vol. 3, no. 9, pp. 329–336, 1999.
- [26] F. Steinicke, G. Bruder, J. Jerald, H. Frenz, and M. Lappe, “Analyses of human sensitivity to redirected walking,” in *Proceedings of the 2008 ACM symposium on Virtual reality software and technology*, 2008, pp. 149–156.
- [27] K.-L. Besser and E. A. Jorswieck, “Reconfigurable intelligent surface phase hopping for ultra-reliable communications,” *IEEE Transactions on Wireless Communications*, vol. 21, no. 11, pp. 9082–9095, 2022.

- [28] C. Chaccour, M. N. Soorki, W. Saad, M. Bennis, and P. Popovski, “Risk-based optimization of virtual reality over terahertz reconfigurable intelligent surfaces,” in *ICC 2020-2020 IEEE International Conference on Communications (ICC)*, IEEE, 2020, pp. 1–6.
- [29] Y. Zhou, C. Pan, P. L. Yeoh, K. Wang, Z. Ma, B. Vucetic, and Y. Li, “Latency minimization for secure intelligent reflecting surface enhanced virtual reality delivery systems,” *IEEE Wireless Communications Letters*, vol. 11, no. 9, pp. 1770–1774, 2022.
- [30] F. Lemic, J. Martin, C. Yarp, D. Chan, V. Handziski, R. Brodersen, G. Fettweis, A. Wolisz, and J. Wawrzynek, “Localization as a feature of mmwave communication,” in *2016 International Wireless Communications and Mobile Computing Conference (IWCMC)*, IEEE, 2016, pp. 1033–1038.
- [31] M. Ruble and I. Güvenç, “Wireless localization for mmwave networks in urban environments,” *EURASIP journal on advances in signal processing*, vol. 2018, no. 1, pp. 1–19, 2018.
- [32] N. N. Bhat, R. Berkvens, and J. Famaey, “Gesture recognition with mmwave wi-fi access points: Lessons learned,” in *2023 IEEE 24th International Symposium on a World of Wireless, Mobile and Multimedia Networks (WoWMoM)*, IEEE, 2023, pp. 127–136.
- [33] P. Talarn, B. Ollé, F. Lemic, S. Abadal, and X. Costa-Perez, “Real-time generation of 3-dimensional representations of static objects using small unmanned aerial vehicles,” in *Proceedings of the 29th Annual International Conference on Mobile Computing and Networking*, 2023, pp. 1–3.
- [34] Z.-M. Jiang, M. Rihan, P. Zhang, L. Huang, Q. Deng, J. Zhang, and E. M. Mohamed, “Intelligent reflecting surface aided dual-function radar and communication system,” *IEEE Systems Journal*, vol. 16, no. 1, pp. 475–486, 2021.
- [35] R. S. Prasobh Sankar, B. Deepak, and S. P. Chepuri, “Joint communication and radar sensing with reconfigurable intelligent surfaces,” in *2021 IEEE 22nd International Workshop on Signal Processing Advances in Wireless Communications (SPAWC)*, 2021, pp. 471–475.
- [36] R. Li, X. Shao, S. Sun, M. Tao, and R. Zhang, “Beam scanning for integrated sensing and communication in irs-aided mmwave systems,” in *2023 IEEE 24th International Workshop on Signal Processing Advances in Wireless Communications (SPAWC)*, IEEE, 2023, pp. 196–200.
- [37] X. Hu, C. Liu, M. Peng, and C. Zhong, “Irs-based integrated location sensing and communication for mmwave simo systems,” *IEEE Transactions on Wireless Communications*, vol. 22, no. 6, pp. 4132–4145, 2023.
- [38] Y. Sun, Z. Huang, H. Zhang, Z. Cao, and D. Xu, “3drimr: 3d reconstruction and imaging via mmwave radar based on deep learning,” in *2021 IEEE International Performance, Computing, and Communications Conference (IPCCC)*, IEEE, 2021, pp. 1–8.
- [39] H. Guo, N. Zhang, W. Shi, A.-A. Saeed, S. Wu, and H. Wang, “Real-time indoor 3d human imaging based on mimo radar sensing,” in *2019 IEEE International Conference on Multimedia and Expo (ICME)*, IEEE, 2019, pp. 1408–1413.
- [40] X. Hu, N. Tong, Y. Guo, and S. Ding, “Mimo radar 3-d imaging based on multi-dimensional sparse recovery and signal support prior information,” *IEEE Sensors Journal*, vol. 18, no. 8, pp. 3152–3162, 2018.

- [41] W. He, K. Wu, Y. Zou, and Z. Ming, “Wig: Wifi-based gesture recognition system,” in *2015 24th International Conference on Computer Communication and Networks (ICCCN)*, IEEE, 2015, pp. 1–7.
- [42] R. H. Venkatnarayan, G. Page, and M. Shahzad, “Multi-user gesture recognition using wifi,” in *Proceedings of the 16th Annual International Conference on Mobile Systems, Applications, and Services*, 2018, pp. 401–413.
- [43] Y. Ren, J. Lu, A. Beletchi, Y. Huang, I. Karmanov, D. Fontijne, C. Patel, and H. Xu, “Hand gesture recognition using 802.11 ad mmwave sensor in the mobile device,” in *2021 IEEE Wireless Communications and Networking Conference Workshops (WCNCW)*, IEEE, 2021, pp. 1–6.
- [44] W. Jiang, C. Miao, F. Ma, S. Yao, Y. Wang, Y. Yuan, H. Xue, C. Song, X. Ma, D. Koutsonikolas, *et al.*, “Towards environment independent device free human activity recognition,” in *Proceedings of the 24th annual international conference on mobile computing and networking*, 2018, pp. 289–304.
- [45] J. Zhang, Z. Tang, M. Li, D. Fang, P. Nurmi, and Z. Wang, “Crosssense: Towards cross-site and large-scale wifi sensing,” in *Proceedings of the 24th annual international conference on mobile computing and networking*, 2018, pp. 305–320.
- [46] Y. Zheng, Y. Zhang, K. Qian, G. Zhang, Y. Liu, C. Wu, and Z. Yang, “Zero-effort cross-domain gesture recognition with wi-fi,” in *Proceedings of the 17th annual international conference on mobile systems, applications, and services*, 2019, pp. 313–325.
- [47] W. Jiang, H. Xue, C. Miao, S. Wang, S. Lin, C. Tian, S. Murali, H. Hu, Z. Sun, and L. Su, “Towards 3d human pose construction using wifi,” in *Proceedings of the 26th Annual International Conference on Mobile Computing and Networking*, 2020, pp. 1–14.
- [48] Y. Ren, Z. Wang, S. Tan, Y. Chen, and J. Yang, “Winect: 3d human pose tracking for free-form activity using commodity wifi,” *Proceedings of the ACM on Interactive, Mobile, Wearable and Ubiquitous Technologies*, vol. 5, no. 4, pp. 1–29, 2021.
- [49] B. Mildenhall, P. P. Srinivasan, M. Tancik, J. T. Barron, R. Ramamoorthi, and R. Ng, “Nerf: Representing scenes as neural radiance fields for view synthesis,” *Communications of the ACM*, vol. 65, no. 1, pp. 99–106, 2021.
- [50] B. Kerbl, G. Kopanas, T. Leimkühler, and G. Drettakis, “3d gaussian splatting for real-time radiance field rendering,” *ACM Transactions on Graphics*, vol. 42, no. 4, pp. 1–14, 2023.
- [51] S. Mohebi, M. Lecci, A. Zanella, and M. Zorzi, “The challenges of scheduling and resource allocation in ieee 802.11ad/ay,” in *2020 Mediterranean Communication and Computer Networking Conference*, 2020, pp. 1–4.
- [52] P. Saxena and A. Kothari, “Performance analysis of adaptive beamforming algorithms for smart antennas,” *IERI Procedia*, vol. 10, pp. 131–137, 2014.
- [53] W. Tang, M. Z. Chen, X. Chen, J. Y. Dai, Y. Han, M. Di Renzo, Y. Zeng, S. Jin, Q. Cheng, and T. J. Cui, “Wireless communications with reconfigurable intelligent surface: Path loss modeling and experimental measurement,” *IEEE Transactions on Wireless Communications*, vol. 20, no. 1, pp. 421–439, 2021.
- [54] E. Björnson and L. Sanguinetti, “Power scaling laws and near-field behaviors of massive mimo and intelligent reflecting surfaces,” *IEEE Open Journal of the Communications Society*, vol. 1, pp. 1306–1324, 2020.

- [55] Z. Yu, X. Hu, C. Liu, M. Peng, and C. Zhong, “Location sensing and beamforming design for irs-enabled multi-user isac systems,” *IEEE Transactions on Signal Processing*, vol. 70, pp. 5178–5193, 2022.
- [56] S. Gong, C. Xing, P. Yue, L. Zhao, and T. Q. S. Quek, “Hybrid analog and digital beamforming for ris-assisted mmwave communications,” *IEEE Transactions on Wireless Communications*, vol. 22, no. 3, pp. 1537–1554, 2023.
- [57] K. Li, M. Cui, G. Zhang, Q. Wu, D. Li, and J. He, “Robust transmit and reflect beamforming design for irs-assisted offshore noma communication systems,” *IEEE Transactions on Vehicular Technology*, vol. 73, no. 1, pp. 783–798, 2024.
- [58] G.-H. Li, D.-W. Yue, and S.-N. Jin, “Spatially correlated rayleigh fading characteristics of ris-aided mmwave mimo communications,” *IEEE Communications Letters*, vol. 27, no. 8, pp. 2222–2226, 2023.
- [59] J. Jalali, F. Lemic, H. Tabassum, R. Berkvens, and J. Famaey, “Toward energy efficient multiuser irs-assisted urllc systems: A novel rank relaxation method,” in *2023 IEEE Globecom Workshops (GC Wkshps)*, 2023, pp. 1354–1360.
- [60] K. Ntontin, D. Selimis, A.-A. A. Boulogeorgos, A. Alexandridis, A. Tsolis, V. Vlachodimitropoulos, and F. Lazarakis, “Optimal reconfigurable intelligent surface placement in millimeter-wave communications,” in *2021 15th European Conference on Antennas and Propagation (EuCAP)*, IEEE, 2021, pp. 1–5.
- [61] Ö. Özdogan, E. Björnson, and E. G. Larsson, “Intelligent reflecting surfaces: Physics, propagation, and pathloss modeling,” *IEEE Wireless Communications Letters*, vol. 9, no. 5, pp. 581–585, 2019.
- [62] V. Angelov, E. Petkov, G. Shipkovenski, and T. Kalushkov, “Modern virtual reality headsets,” in *2020 International congress on human-computer interaction, optimization and robotic applications (HORA)*, IEEE, 2020, pp. 1–5.
- [63] F. Lemic, J. Struye, and J. Famaey, “User mobility simulator for full-immersive multiuser virtual reality with redirected walking,” in *Proceedings of the 12th ACM Multimedia Systems Conference*, 2021, pp. 293–299.